J. Fluid Mech. (1990), *vol.* 213, *pp.* 443–464
Printed in Great Britain

Recirculating pipe flows

By D. B. INGHAM,[1] D. J. KEEN,[1] P. J. HEGGS[2] AND B. R. MORTON[3]

[1] Department of Applied Mathematical Studies, University of Leeds, Leeds, LS2 9JT, UK
[2] Department of Chemical Engineering, University of Bradford, Bradford, BD7 1DP, UK
[3] Department of Mathematics, Monash University, Clayton, Victoria, 3168, Australia

(Received 17 January 1989 and in revised form 16 September 1989)

Experimental and numerical investigations are performed for the situation of steady recirculating combined-convection water flows in a cylindrical duct. The experimental results are presented as photographs from which information regarding the stream-function and temperature distributions within the water can be deduced. The experimental flows, which have Reynolds number in the range $15 < Re < 31$, are modelled numerically using an elliptic finite-difference formulation and a multigrid solution technique. The results for stream function and temperature are compared with the experimental results and agreement is found to be generally very good. Plots of flow average temperature, local Nusselt number, average Nusselt number and friction factor times Reynolds number are also presented for each flow situation considered.

1. Introduction

The problem of obtaining both numerical and experimental flow patterns for axisymmetric, steady, laminar, recirculating flows in vertical pipes subject to heating and/or cooling of wall sections has been considered recently by Morton *et al.* (1987). These flows are of great interest because of their general relevance to the modelling of heat exchangers in industry and the cooling processes in nuclear reactors, to take two applications, but equally for the insight they offer into flows under competing distributions of internal force. Although the pressure differences between pipe ends may seem large, interior pressure gradients are small and can readily be matched by buoyancy forces, producing in some parts of the flow forward acceleration and in others reversed acceleration. These are problems of mixed convection, combining aspects of forced convection in response to the externally imposed pressure gradients, typically characterized by a Reynolds number, with free convection responding to the buoyancy forces arising from the temperature distributions, characterized by a Grashof (or equally a Rayleigh) number. Moreover the inter-relationship of the velocity and temperature fields depends on the Prandtl number. With these three parameters in addition to any geometric ratios a rich variety of flows and temperature states may be achieved. Some years ago, one of the present authors gave a very simple asymptotic solution for flow up a uniformly heated vertical pipe (Morton 1960), demonstrating a balance of pressure gradient, buoyancy and viscous forces that could drive steady axial downflow surrounded by an annulus of upflow. The possibility of axial stagnation was clear at the time, but it has taken major improvements in computing and numerical capabilities to treat

realistic problems involving entry length flows and the response of flows to various changes in heating and cooling of the pipe wall.

A preliminary discussion of some cases of interior flow stagnation and flow reversal has already been presented, and in this paper the numerical and experimental investigations are studied in greater detail over a wider range of parameters. The experimental aspects are substantially improved over the earlier work, both to cover a more representative set of interior flows, and in the use of temperature-sensitive liquid crystal capsules which provide reasonable detail on the temperature fields within the flow.

Another aim of the paper is to introduce multigrid techniques in order to accelerate the numerical solution of the finite-difference problem considered. Multigrid methods are a relatively recent area of research and have only been brought into real prominence since the publication of the major piece of work on the subject by Brandt (1977). Since then an increasing amount of work has been carried out on the subject, with particular attention being given to 'lid-driven cavity' flows in the papers of Ghia, Ghia & Shin (1982), Phillips & Schmidt (1985), Fuchs (1986) and Gaskell, Lau & Wright (1988). In this paper the basic multigrid concepts are considered and a method of application similar to those used by Falle & Wilson (1988) and Gaskell *et al.* (1988) is used to solve the problem under consideration. Significant improvement in the computation time required for the convergence of the solution of the finite-difference equations on the finest mesh is achieved. As a consequence a much finer mesh is used than in the previously reported calculations of Morton *et al.*, thus enabling more accurate solutions to be presented. A comparison between the results obtained in the numerical and experimental investigations reveals very good correspondence, and an examination of the numerical solutions reveals new information with regard to the flow structure and heat transfer of the experimental situations.

The intention in this paper is to provide a widely representative set of interior flows using improved computing techniques that will handle the temperature singularities at the walls and improved experimental techniques that will give a sufficient approximation to the temperature fields. In this way wider attention can be drawn to this interesting set of interior flows.

2. Experimental set-up

The experimental apparatus, which is illustrated schematically in figure 1, consists of a length of thin-walled vertical Perspex tube (A), encased by a two-section water bath. The water bath consists of independent sections, (B) and (C), each with thin end plates drilled precisely to give a direct seal against the experimental tube (A), thus minimizing the thermal impedance between bath water and experimental fluid. In operation the baths (B) and (C) are separated by a small air (or other insulating material) gap and water at the required temperature is circulated at rates very much greater than the rate at which water passes through the vertical tube (A). This ensures that the bath sections of the tube (A) will respond closely to both temperatures when steady flow is achieved, except for short lengths of order the pipe wall thickness at the ends of the baths. In view of the difficulty in determining precise temperature fields from the liquid crystal display, it was felt that this was sufficient and measurements of the inner wall temperatures were not attempted as the intention was to provide descriptions of reasonable accuracy over a wide range of interesting flows rather than to concentrate on precise details for a single flow.

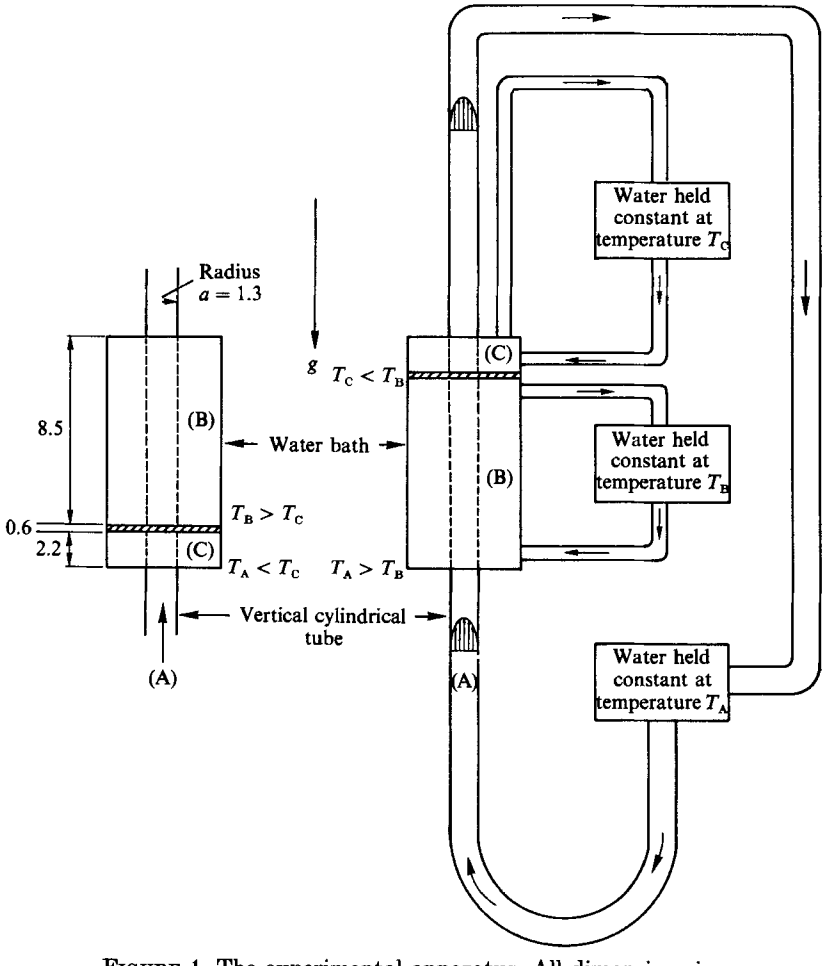

FIGURE 1. The experimental apparatus. All dimensions in mm.

The dimensions of the water bath are as indicated in figure 1. When it is desired to first cool and then heat the water flowing up the tube, the water bath is positioned so that the short section (C) is placed below the long section (B) and T_C is chosen to be less than both T_A and T_B. However, if it is desired to first heat the water in the tube, the bath may be positioned either with the short section (C) below the long section (B), with the temperatures being maintained so that $T_A < T_C$ and $T_B < T_C$, or with (B) below (C) with the temperatures being maintained so that $T_A < T_B$ and $T_C < T_B$. The reason for having both heating and cooling sections in the water bath is to restrict any recirculation regions formed in the first section of the bath, thus assisting the experimental flows to remain stable. The shorter section is used for cooling when the water is first cooled because it is difficult to maintain a steady flow when the recirculation region adjacent to the duct wall becomes too large. The water streams being pumped up the vertical tube and into the two water baths are maintained at constant temperatures by storing prior to pumping in tanks which are held at specified temperatures. The temperature T_A is very close to the temperature of the room so that little or no heat transfer can take place until the water enters the section of the tube encased by the water bath. The straight length of tube, preceding the heat transfer region, is long enough so that fully developed flow can be set up

before the fluid velocity is affected by the heat transfer region. Beyond the region encased by the water bath there is a long length of straight vertical pipe where the fluid velocity is able to return to that of fully developed flow. The average velocities for each individual situation were found by using a flow meter which was situated in the section of the pipe preceding the heat transfer region. Colour photographs are presented from these experimental investigations from which a certain amount of information regarding the streamlines and temperature distributions within the water can be deduced. The streamlines were revealed by adding aluminium powder to the water in the tube and the temperature distribution within the fluid can be seen because encapsulated liquid crystals are dispersed in the water which change colour from red through yellow and blue to purple over a temperature range of approximately 22.0–27.0 °C. These substances are sufficiently small (2–50 μm) and in low concentrations so as not to change any of the physical properties of the water. Photographs are presented from several investigations and comparisons are made as the governing parameters Re, Gr/Re and θ_∞ (see §3 for definitions) are allowed to vary.

3. General numerical theory

Steady laminar combined convection of a fluid with velocity (v, u) inside a vertical circular tube of radius a as illustrated in figure 2 is the situation under consideration. In the model an entry section between $z = 0$ and $z = b$ is employed where the temperature of the wall for $0 < z < b$ is held constant at $T = T_e$. The value of b is chosen so that the boundary condition at $z = 0$ is a good approximation to $z = -\infty$ where fully developed parabolic flow, $(0, u_e)$, at constant temperature is assumed. A heated/cooled section is situated between $z = b$ and $z = c$ where the temperature of the tube wall is maintained at $T = T_h$ and beyond $z = c$ the temperature of the wall is reduced/increased to T_∞ which is the temperature that the fluid attains as z tends to infinity. It should be noted at this point that in the mathematical model the region beyond the second section of the water bath is being treated as if that part of the bath extends to infinity. This is a fair assumption to make for both configurations of the water bath for the following reasons. In the situation where the large section of the bath is uppermost it is reasonable to assume that most of the heat transfer takes place inside the length of the tube encased by the water bath, and in the situation where the small section is uppermost the fluid is heated in the large section of the water bath and cooled in the small section to a temperature which is very similar to the room temperature. No changes occur in the azimuthal direction so the solution domain can be reduced to $0 < r < a$, $0 < z < \infty$ where a is the radius of the tube and the condition $\partial/\partial r \equiv 0$ applies along $r = 0$. The acceleration due to gravity, g, acts vertically downwards in the opposite direction to the forced convection. The fluid is considered to be Newtonian with constant dynamic viscosity, thermal conductivity, specific heat capacity and coefficient of expansion. Density variations are assumed to be negligible except in the buoyancy term of the vertical momentum equation (Boussinesq approximation). Gray & Giorgini (1976) have questioned the validity of the Boussinesq approximation when solving a related problem involving Bénard convection. They conclude that for Bénard convection the Boussinesq approximation is valid for water at the ambient temperature 15 °C when typical temperature differences are $\leqslant 1.25$ °C. In this investigation it has been assumed that the Boussinesq approximation is valid despite the fact that temperature differences up

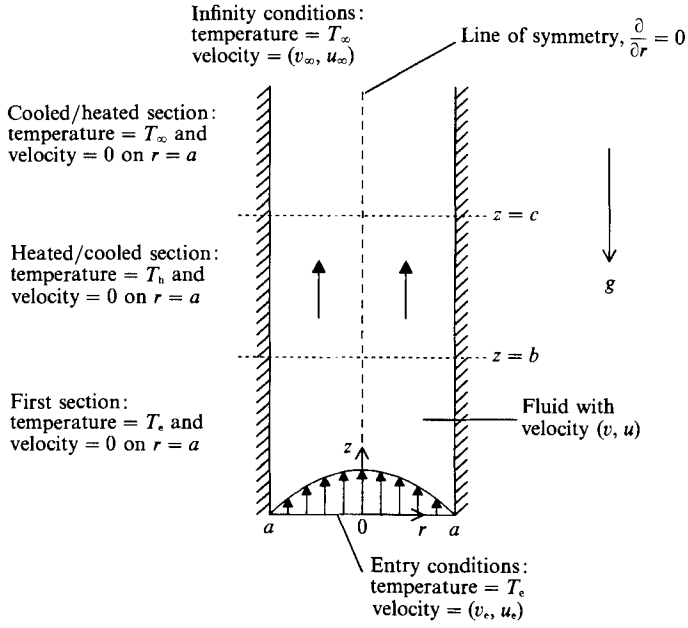

FIGURE 2. Illustration of the convection system under consideration.

to 3.7 °C exist. The flow situation is vastly different to that investigated by Gray & Giorgini and, since the agreement found between the numerical and experimental investigations is good, it has been assumed that it is reasonable to use the Boussinesq approximation here. However, if more detailed comparisons are to be made, then temperature variations in all physical properties would clearly improve the numerical model. The above assumptions are made in order to keep the model as simple as possible, although inclusion of variations in some of the physical parameters should not in theory be difficult to introduce into the following numerical theory. Viscous dissipation is ignored in the energy equation as it was shown to have only a small effect by Collins (1975).

The governing equations are the continuity, axial momentum, radial momentum and energy equations and these can be written in the form (Morton *et al.* 1987)

$$\frac{\partial u}{\partial z}+\frac{\partial v}{\partial r}+\frac{v}{r}=0, \tag{1}$$

$$u\frac{\partial u}{\partial z}+v\frac{\partial u}{\partial r}=-\frac{1}{\rho}\frac{\partial p}{\partial z}+\nu\left[\frac{\partial^2 u}{\partial z^2}+\frac{1}{r}\frac{\partial}{\partial r}\left(r\frac{\partial u}{\partial r}\right)\right]-g, \tag{2}$$

$$u\frac{\partial v}{\partial z}+v\frac{\partial v}{\partial r}=-\frac{1}{\rho}\frac{\partial p}{\partial r}+\nu\left[\frac{\partial^2 v}{\partial z^2}+\frac{1}{r}\frac{\partial}{\partial r}\left(r\frac{\partial v}{\partial r}\right)-\frac{v}{r^2}\right], \tag{3}$$

$$u\frac{\partial T}{\partial z}+v\frac{\partial T}{\partial r}=\alpha\left[\frac{\partial^2 T}{\partial z^2}+\frac{1}{r}\frac{\partial}{\partial r}\left(r\frac{\partial T}{\partial r}\right)\right], \tag{4}$$

where α is the molecular thermal diffusivity, ν the kinematic viscosity, ρ the density

and p the pressure of the fluid. The boundary conditions for the problem are as follows:

$$\text{at } r = 0, \quad 0 < z < \infty: \quad v = 0, \quad \frac{\partial u}{\partial r} = 0, \quad \frac{\partial T}{\partial r} = 0; \tag{5}$$

$$\left.\begin{aligned} \text{at } r = a, \quad 0 \leqslant z < \infty: \quad & v = 0, \quad u = 0, \\ 0 \leqslant z < b: \quad & T = T_e, \\ b \leqslant z < c: \quad & T = T_h, \\ c \leqslant z < \infty: \quad & T = T_\infty; \end{aligned}\right\} \tag{6}$$

$$\text{at } z = 0, \quad 0 \leqslant r \leqslant a: \quad v = 0, \quad u = u_e, \quad T = T_e; \tag{7}$$

$$\text{as } z \to \infty, \quad 0 \leqslant r \leqslant a: \quad v = 0, \quad u = u_\infty, \quad T = T_\infty. \tag{8}$$

The velocities $u_e = u_\infty$ correspond to parabolic velocity profiles.

The Boussinesq approximation involves replacing ρ by $\rho_0[1-\beta(T-T_e)]$ in the buoyancy term of (2) and by ρ_0 elsewhere. Here $\beta = (-1/\rho)(\partial\rho/\partial T)$ is the coefficient of expansion with respect to T, and ρ_0 is the density at $T = T_e$. The non-dimensional variables V, U, R, Z, P and θ are defined as follows:

$$\left.\begin{aligned} & v = u_m V, \quad u = u_m U, \quad r = aR, \quad z = a\,Re\,Z, \\ & p = g\rho_0 z[\beta(T_h - T_e) - 1] + \rho_0 u_m^2 P, \quad T = T_h + (T_e - T_h)\theta, \end{aligned}\right\} \tag{9}$$

where u_m is a characteristic velocity taken in this study to be the mean velocity and $Re = au_m/\nu$ is the Reynolds number. Now introduce a stream function, ψ, which satisfies the continuity equation (1):

$$V = \frac{1}{Re}\frac{1}{R}\frac{\partial\psi}{\partial Z}, \quad U = -\frac{1}{R}\frac{\partial\psi}{\partial R}, \tag{10}$$

and define the vorticity as follows:

$$\Omega = \frac{1}{Re}\frac{\partial V}{\partial Z} - \frac{\partial U}{\partial R}. \tag{11}$$

Combining (10) and (11) leads to

$$\Omega R = \frac{1}{Re^2}\frac{\partial^2\psi}{\partial Z^2} + \frac{\partial^2\psi}{\partial R^2} - \frac{1}{R}\frac{\partial\psi}{\partial R}, \tag{12}$$

and if P is eliminated between (2) and (3), (2)–(4) become

$$\frac{1}{R}\frac{\partial\psi}{\partial Z}\frac{\partial\Omega}{\partial R} - \frac{1}{R}\frac{\partial\psi}{\partial R}\frac{\partial\Omega}{\partial Z} - \frac{\Omega}{R^2}\frac{\partial\psi}{\partial Z} = \frac{1}{Re^2}\frac{\partial^2\Omega}{\partial Z^2} + \frac{\partial^2\Omega}{\partial R^2} + \frac{1}{R}\frac{\partial\Omega}{\partial R} - \frac{\Omega}{R^2} - \frac{Gr}{Re}\frac{\partial\theta}{\partial R}, \tag{13}$$

$$\frac{1}{R}\frac{\partial\psi}{\partial Z}\frac{\partial\theta}{\partial R} - \frac{1}{R}\frac{\partial\psi}{\partial R}\frac{\partial\theta}{\partial Z} = \frac{1}{Pr}\left\{\frac{1}{Re^2}\frac{\partial^2\theta}{\partial Z^2} + \frac{\partial^2\theta}{\partial R^2} + \frac{1}{R}\frac{\partial\theta}{\partial R}\right\}, \tag{14}$$

where $Pr = \nu/\alpha$ is the Prandtl number, and $Gr = g\beta(T_e - T_h)a^3/\nu^2$ is the Grashof number. The boundary conditions (5)–(8) become

$$\text{at } R = 0, \quad 0 \leqslant Z < \infty: \quad \psi = 0.5, \quad \Omega = 0, \quad \frac{\partial\theta}{\partial R} = 0; \tag{15}$$

$$\left.\begin{aligned} &\text{at } R=1, \quad 0\leqslant Z<\infty: \quad \psi=0, \quad \frac{\partial\psi}{\partial R}=0,\\ &\qquad\qquad 0\leqslant Z<b/aRe: \quad \theta=1,\\ &\qquad\qquad b/aRe\leqslant Z<c/aRe: \quad \theta=0,\\ &\qquad\qquad c/aRe\leqslant Z<\infty: \quad \theta=\theta_\infty; \end{aligned}\right\} \tag{16}$$

$$\text{at } Z=0, \quad 0\leqslant R\leqslant 1: \quad \psi=\tfrac{1}{2}(1-R^2)^2, \quad \Omega=4R, \quad \theta=1; \tag{17}$$

$$\text{as } Z\to\infty, \quad 0\leqslant R\leqslant 1: \quad \psi=\tfrac{1}{2}(1-R^2)^2, \quad \Omega=4R, \quad \theta=\theta_\infty; \tag{18}$$

where $\theta_\infty=(T_\infty-T_h)/(T_e-T_h)$.

The elliptic equations (12)–(14) give the desired description of the flow under consideration and these must be solved subject to the boundary conditions (15)–(18). Such a solution is obtained by expressing the governing equations in finite-difference form and solving them iteratively on a given fine grid with the aid of corrections from coarser grids which accelerate the rate of convergence of a relaxation scheme on the finest grid by efficiently smoothing error components (multigrade methods).

In order to satisfy boundary condition (18) a scaling is used in the axial direction. This scaling is applied only over the region $d<Z<\infty$ where $Z=d$ is a station in the range 6–13 pipe diameters downstream of $Z=0$, depending upon the magnitude of Re. The scaling of the axial coordinate, as used by Morton *et al.* (1987), is defined as follows:

$$\xi=1-1/(1+C(Z-d)) \quad \text{or} \quad Z=(\xi/C)/(1-\xi)+d, \tag{19}$$

where ξ is a new axial variable which lies in the range $0\leqslant\xi\leqslant 1$ and C is a transformation parameter to be defined later. Equations (12)–(14) under this transformation become

$$\Omega R=\frac{1}{Re^2}\left[\frac{\partial^2\psi}{\partial\xi^2}\left(\frac{d\xi}{dZ}\right)^2+\frac{\partial\psi}{\partial\xi}\frac{d^2\xi}{dZ^2}\right]+\frac{\partial^2\psi}{\partial R^2}-\frac{1}{R}\frac{\partial\psi}{\partial R}, \tag{20}$$

$$\frac{1}{R}\frac{d\xi}{dZ}\left[\frac{\partial\psi}{\partial\xi}\frac{\partial\Omega}{\partial R}-\frac{\partial\psi}{\partial R}\frac{\partial\Omega}{\partial\xi}-\frac{\Omega}{R}\frac{\partial\psi}{\partial\xi}\right]=\frac{1}{Re^2}\left[\frac{\partial^2\Omega}{\partial\xi^2}\left(\frac{d\xi}{dZ}\right)^2+\frac{\partial\Omega}{\partial\xi}\frac{d^2\xi}{dZ^2}\right]+\frac{\partial^2\Omega}{\partial R^2}+\frac{1}{R}\frac{\partial\Omega}{\partial R}-\frac{\Omega}{R^2}-\frac{Gr}{Re}\frac{\partial\theta}{\partial R}, \tag{21}$$

$$\frac{1}{R}\frac{d\xi}{dz}\left[\frac{\partial\psi}{\partial\xi}\frac{\partial\theta}{\partial R}-\frac{\partial\psi}{\partial R}\frac{\partial\theta}{\partial\xi}\right]=\frac{1}{Pr}\left\{\frac{1}{Re^2}\left[\frac{\partial^2\theta}{\partial\xi^2}\left(\frac{d\xi}{dZ}\right)^2+\frac{\partial\theta}{\partial\xi}\frac{d^2\xi}{dZ^2}\right]+\frac{\partial^2\theta}{\partial R^2}+\frac{1}{R}\frac{\partial\theta}{\partial R}\right\}. \tag{22}$$

The solution domain of the problem can now be split into two regions, namely $0\leqslant Z\leqslant d$ where (12)–(17) are expressed in finite-difference form on a fine regular rectangular grid, G^Z, of $N+1$ points in the radial direction and $NN+1$ points in the axial direction, and $d\leqslant Z<\infty$ where (20)–(22), (15), (16) and (18) are expressed in finite-difference form on a fine regular rectangular grid, G^ξ, of $N+1$ points in the radial direction and $N^\xi+1$ points in the ξ-direction. The value of the parameter C is chosen so that the step size between the axial locations Z_{NN+2} and $Z_{NN+1}=d$ on G^ξ is the same as the distance between axial locations Z_{NN+1} and Z_{NN} on the fine grid G^Z (the subscript NN refers to values at the NNth axial location). Thus if $\xi_{NN+2}=1/N^\xi=1-1/(1+C(Z_{NN+2}-d))$ and $Z_{NN+2}-Z_{NN+1}=K$ where $K=d/NN$ it must hold that

$$C=1/((N^\xi-1)K) \tag{23}$$

and hence for $Z\geqslant d$,

$$Z=(\xi(N^\xi-1)K)/(1-\xi)+d. \tag{24}$$

Central differences are employed in the radial direction for both first and second derivatives; however, attempts to do the same in the axial direction produce oscillations in the solution. These oscillations arise from the large internal gradients in temperature and velocity; they are absent if Gr/Re is sufficiently small (this would be expected since on the finest mesh the cell Reynolds number in the radial direction is < 0.5 and in the axial direction is < 1.5 for all of the values of Re considered here and central differencing is normally expected to be stable for cell Reynolds numbers up to about 2). The oscillations are overcome by using either backward or forward differencing (first order) in the axial first-derivative terms, depending upon whether the flow at a particular point is in the positive or negative Z-direction, respectively. As Re increases or the flow field becomes more complicated it may be appropriate to use higher-order axial differencing and/or discretization (i.e. adaptive meshing) in the vicinity of the temperature discontinuities. However, for the parameter ranges considered in this paper the relatively small absolute and cell Reynolds numbers involved suggest that any inaccuracies arising from the present formulation will themselves be small.

The vorticity on the boundary is determined to second-order accuracy using Taylor series expansions of Ω and θ at $R = 1$, the fact that $\partial\psi/\partial R = 0$ at $R = 1$, and (12) and (20) evaluated at $R = 1$. The temperature at the centreline is given to second-order accuracy using $\partial\theta/\partial R = 0$ at $R = 0$ and (14) and (22) evaluated at $R = 0$. The finite-difference equations, given in full by Keen (1988), are solved using multigrid techniques and details of the particular scheme used here are given in the Appendix.

Convergence to the exact solution is assumed to have occurred when the average change in the finite-difference variables between consecutive iterations on the finest grid has fallen below 10^{-6}. When the solution procedure is initiated the values given to the finite-difference variables $\psi_{i,j}$ and $\Omega_{i,j}$ (at point (i,j) on the relevant finite-difference grid) correspond to a parabolic velocity profile everywhere, and the values of $\theta_{i,j}$ are put equal to $\theta_{N+1,j}$. If converged solutions already exist and the governing parameters are changed by small amounts then convergence of the new solution may often be achieved more quickly by using this old solution as an initial guess for the new calculation. The values of N and NN are usually taken to be 64 and 256, respectively, with N^{ξ} equal to 256. Calculations with $N = 32$, $NN = 128$ and $N^{\xi} = 128$ suggest that the combined 64×512 grid is fine enough to give an accurate solution and calculations with $N = 96$, $NN = 256$ and $N^{\xi} = 256$ (which is the finest grid possible owing to storage limitations on the computer (Amdahl 5860)) suggest that the results presented here for the stream function are correct to within 1×10^{-3} at every point on the two fine grids G^{Z} and G^{ξ} and colour plots of the temperature distributions for the two finest grids were found to be almost indistinguishable.

In all of the situations considered, the multigrid procedure is seen to speed up the convergence of the solution of the finite-difference equations, and for one typical situation, which was run to convergence on a single grid, the single grid solution took over seven times longer to converge than a multigrid solution using six grids. For more straightforward problems the multigrid techniques employed here would be expected to improve solution times by a factor of $O(10^2)$. However, the temperature singularities encountered in the present study reduce this rate by an order of magnitude. In a related problem with no singularity significantly faster solution times were achieved.

4. Results and comparisons with experiments

Before the more complex flows which provide the basis for this paper are discussed, the original asymptotic solution of an incompressible but thermally responsive fluid under an upward dynamic pressure gradient in a uniformly heated pipe is described. In steady equilibrium flow, if it is assumed that the temperature of both the fluid and inner pipe wall increase linearly with height across the entire fluid section, it may be shown (Morton 1960) that the axial coordinate Z then disappears from the equations, leaving a uniform pressure gradient and a buoyancy force which may be taken as proportional to the local departure of temperature (and hence density) from the section mean. Both pressure gradient and buoyancy are independent of axial height Z, and the pressure gradient is uniform across sections. It follows that buoyancy acts *downwards* against the pressure gradient over the inner part of the pipe section in which temperatures are less than the section mean and *upwards* with the pressure gradient over the remaining outer annulus. For small values of Re and Gr the resulting upward velocity profile is retarded near the axis and broadened towards the walls relative to Poisseuille flow; for somewhat larger values of Re and Gr the upflow can be very significantly reduced near the axis with peak axial flow near the walls and a large increase in pipe impedance; and for larger values of Re and Gr there will be a core of *downward* flow, where negative buoyancy exceeds positive pressure gradient, surrounded by an annulus of upflow near the walls particularly where buoyancy and pressure gradient reinforce. The precise dependence of upward velocity on Re and Gr is complicated, with $U \propto Re\, Gr^{\frac{1}{2}} f(Gr)$, but the essential features of this preliminary discussion are that the pipe flow responds to the local balance between pressure gradient, buoyancy and viscous forces, and that for quite modest heating these forces are of comparable order.

With the laboratory apparatus described in §2, four configurations are possible with cooling followed by heating or heating followed by cooling as the working fluid rises in the vertical tube and with the shorter bath either below or above the longer. Only three of these cases are considered here since flow instability was observed when cooling over the long bath was followed by heating over the short one at much lower values of Re and Gr than in the other three cases. The three other cases are discussed below.

In each case it should be kept in mind that in the *laboratory experiment* T_e is taken as the temperature of the water in the main reservoir and hence of the water entering the working section at the bottom of the lower water bath, T_h is taken as the temperature of the lower water bath, T_∞ as that of the upper water bath, and no special account is taken of temperatures in the vertical tube above the top of the upper water bath. Heat may be lost/gained from this upper section of the pipe surface, although more slowly than in a temperature-controlled bath, and this cooling/heating must be assumed to have some influence on flow at lower levels. In contrast, in the *numerical simulation* the working fluid at $z = 0$ and the wall in $0 < z < b$ is at temperature T_e, the wall temperature in $b < z < c$ is at temperature T_h, and the wall temperature above $z = c$ is maintained at T_∞ without any upper region of cooling/heating. The two problems are very close, but there may be some minor influences from cooling/heating of the upper pipe in the laboratory experiment that are absent from the numerical simulation.

	u_m	T_e	T_h	T_∞	Re	Gr	θ_∞
(*a*)	1.07×10^{-3}	23.4	23.0	26.3	15.1	2442	8.25
(*b*)	1.82×10^{-3}	23.6	23.1	26.2	25.7	3053	6.20
(*c*)	2.24×10^{-3}	23.6	23.1	26.4	31.7	3053	6.60
(*a*)	1.07×10^{-3}	23.8	23.1	26.6	15.1	4273	5.00
(*b*)	1.82×10^{-3}	23.8	23.1	26.7	25.7	4273	5.14
(*c*)	2.24×10^{-3}	23.7	23.1	26.6	31.7	3663	5.83

TABLE 1. Flow data for case (I)

4.1. *Case (I): Cooling over the short section followed by heating over the long section*

For this case the lower bath of length 2.2×10^{-2} m is cooled in each situation by somewhat less than 1 °C below ambient (T_e) and the longer upper bath is warmed by approximately 3 °C above ambient. The parameters ν, β and Pr are given their values at 24 °C, these being 0.92×10^{-6} m^2/s, 2.4×10^{-4} °C^{-1} and 6.3, respectively, as given by Raznjevic (1976). Six situations are considered and the temperature (°C), velocities (m/s) and governing non-dimensional parameters for these flows are displayed in table 1. In figures 3(*a*), 3(*b*) and 3(*c*) (Plate 1), the first three flows in table 1 are displayed in terms of stream function contours from the numerical model, a colour photograph from the experiment and a colour-coded temperature diagram from the numerical model, respectively. The stream-function contours are for ψ in the set $\{-0.14, -0.12, -0.1, \ldots, -0.02, 0, 0.05, 0.1, 0.15, \ldots, 0.4, 0.45, 0.5, 0.505, 0.51, 0.515, \ldots, 0.535, 0.54\}$ where $\psi = 0$ is the streamline along $R = 1$ and $\psi = 0.5$ is the streamline along $R = 0$. The colour coding illustrated was derived from stationary photographs taken over the indicated range of temperatures and is the same for the three colour diagrams. The intention for these three runs was to keep Gr constant and vary Re over the somewhat limited range available. It was not easy to predetermine Gr and the value for figure 3(*a*) came out rather low, although in this case it might be argued that the appropriate Gr should depend upon $T_\infty - T_h$ and hence vary as $\theta_\infty Gr$. The streamline plots reproduce the shapes of the recirculation regions surprisingly well in view of the complexity of the flow. However, the recirculation at the centre of the tube starts a little sooner in the simulation than the experiment for the two larger values of Re in figures 3(*b*) and 3(*c*). It is hard to be certain of the cause of this relatively small difference, but it is possibly due to the differences in treatment of wall temperatures above the second water bath.

The flow and temperature fields are broadly similar in the three cases. The ascending fluid is cooled near the tube wall as it passes through the first bath where buoyancy acts downwards near the wall and upwards near the axis. Flow then enters the heated bath section and a boundary layer of warm fluid grows, with acceleration near the wall, progressive deceleration in a central area and outward radial acceleration of fluid from the axis. In this particular range the flow stagnates on the axis, with the formation of a slowly recirculating core above the stagnation point surrounded by a relatively fast, thin, annular upflow corresponding with the thermal boundary layer. If the simulation were continued sufficiently far upwards, the flow would ultimately reach uniform temperature T_∞ and a parabolic velicity profile some distance above a second axial stagnation point closing the central region of recirculation. Figure 3(*a*) shows the best correspondence between streamlines in the simulation and experiment, but the simulation shows a very weak second

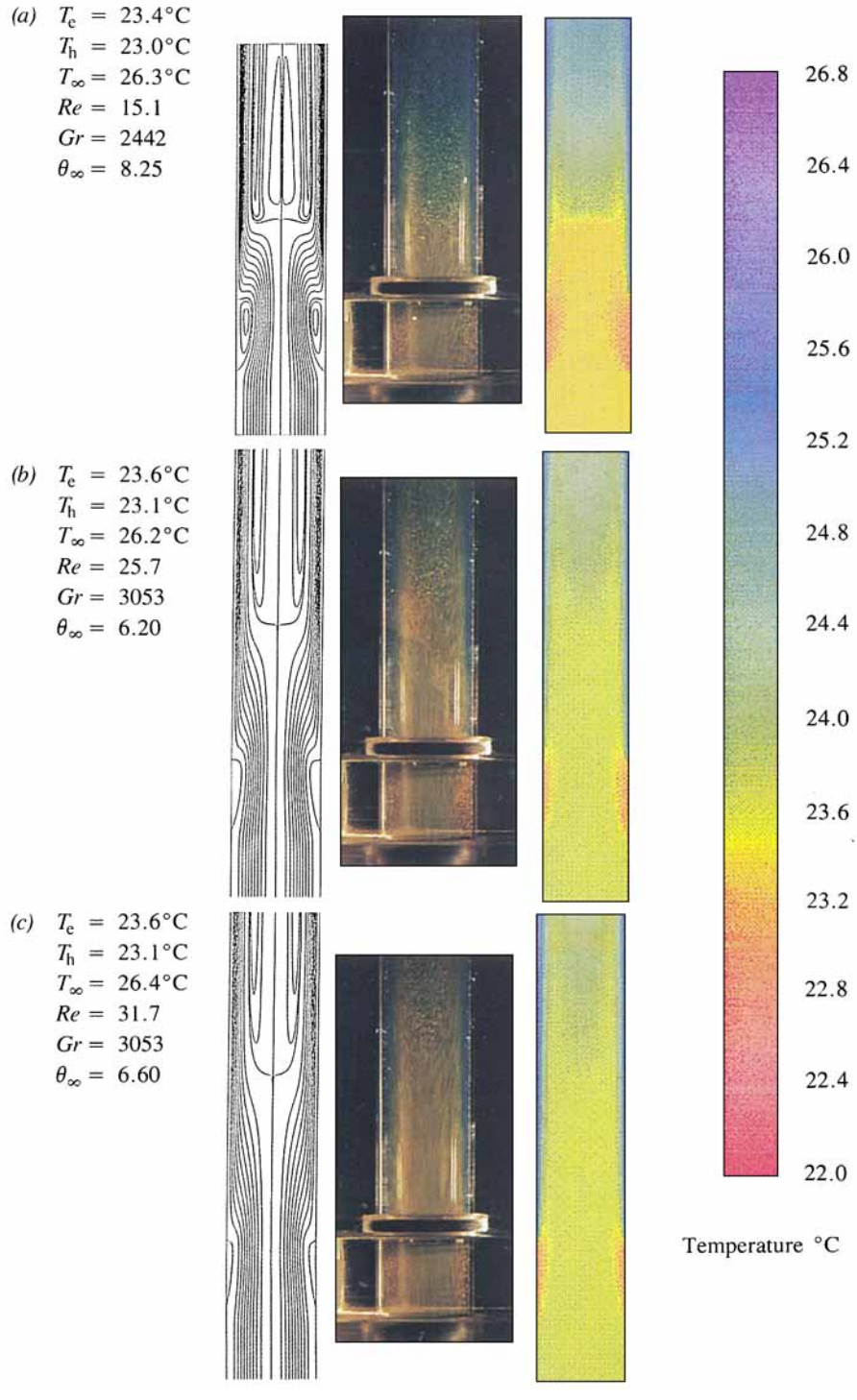

FIGURE 3. Contour plots of stream function, colour photographs from the experiment and colour coded temperature diagrams for the first three flow situations in table 1.

(*Facing p.*452)

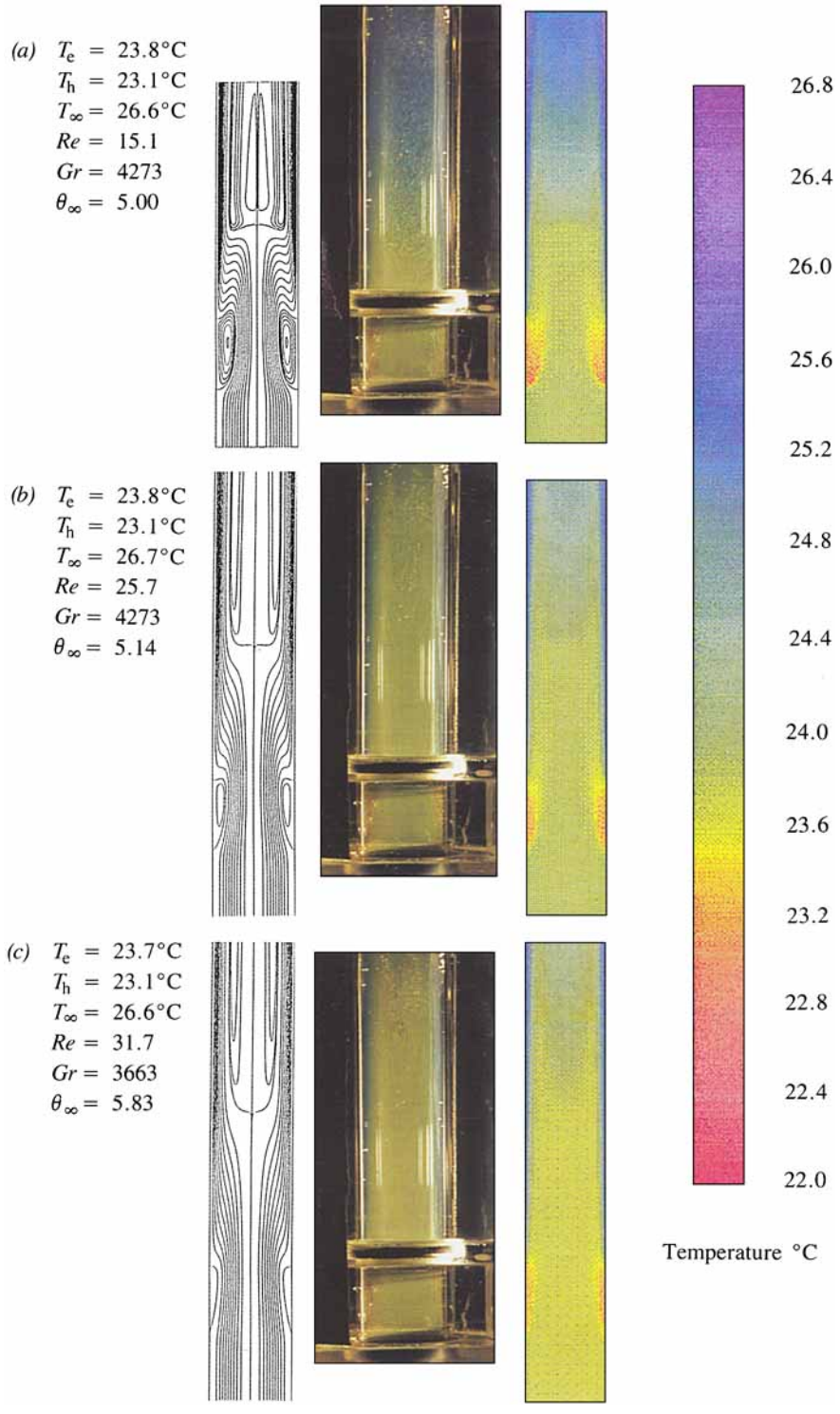

FIGURE 5. Contour plots of stream function, colour photographs from the experiment and colour coded temperature diagrams for the second three flow situations in table 1.

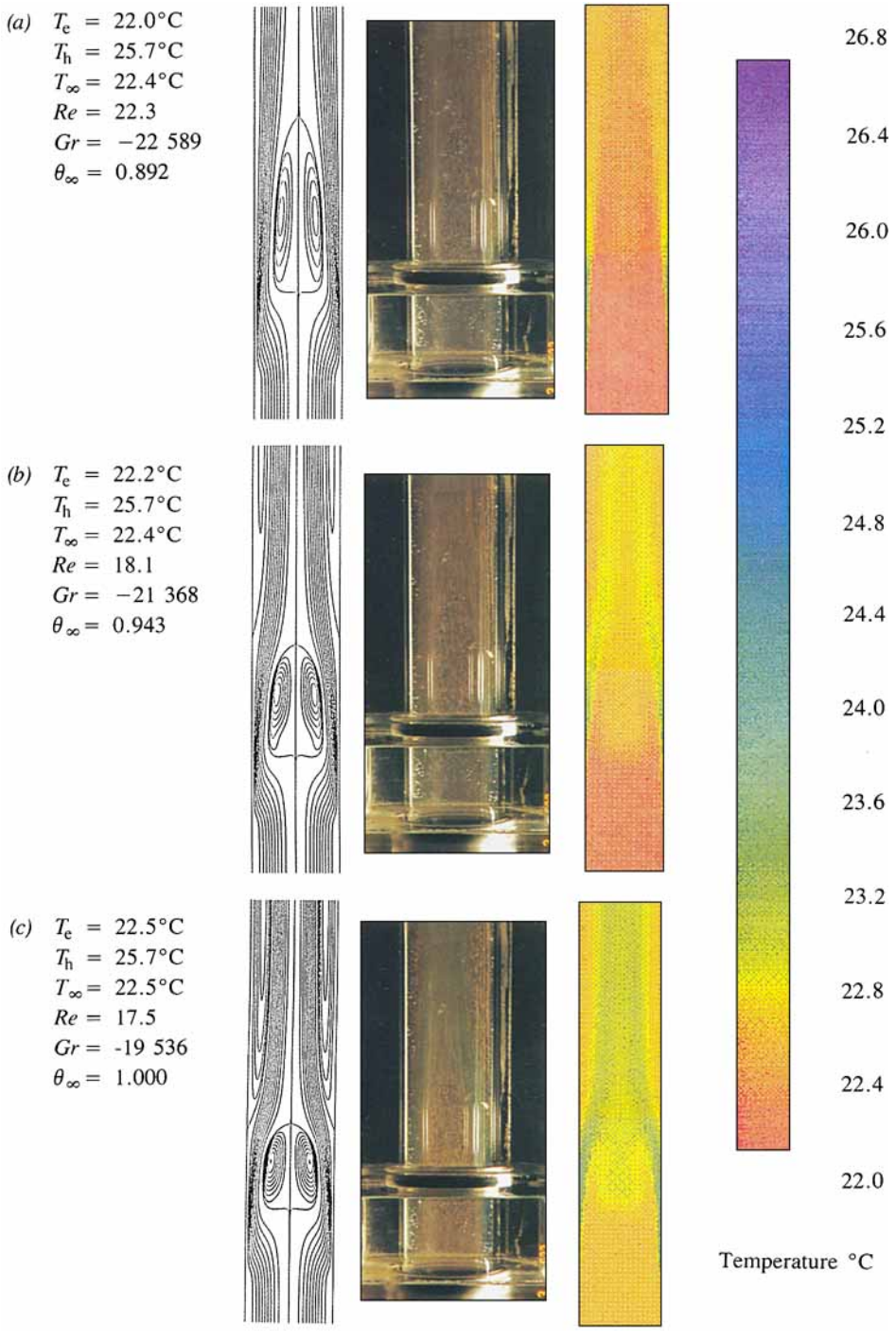

FIGURE 7. Contour plots of stream function, colour photographs from the experiment and colour coded temperature diagrams for the three flow situations in table 2.

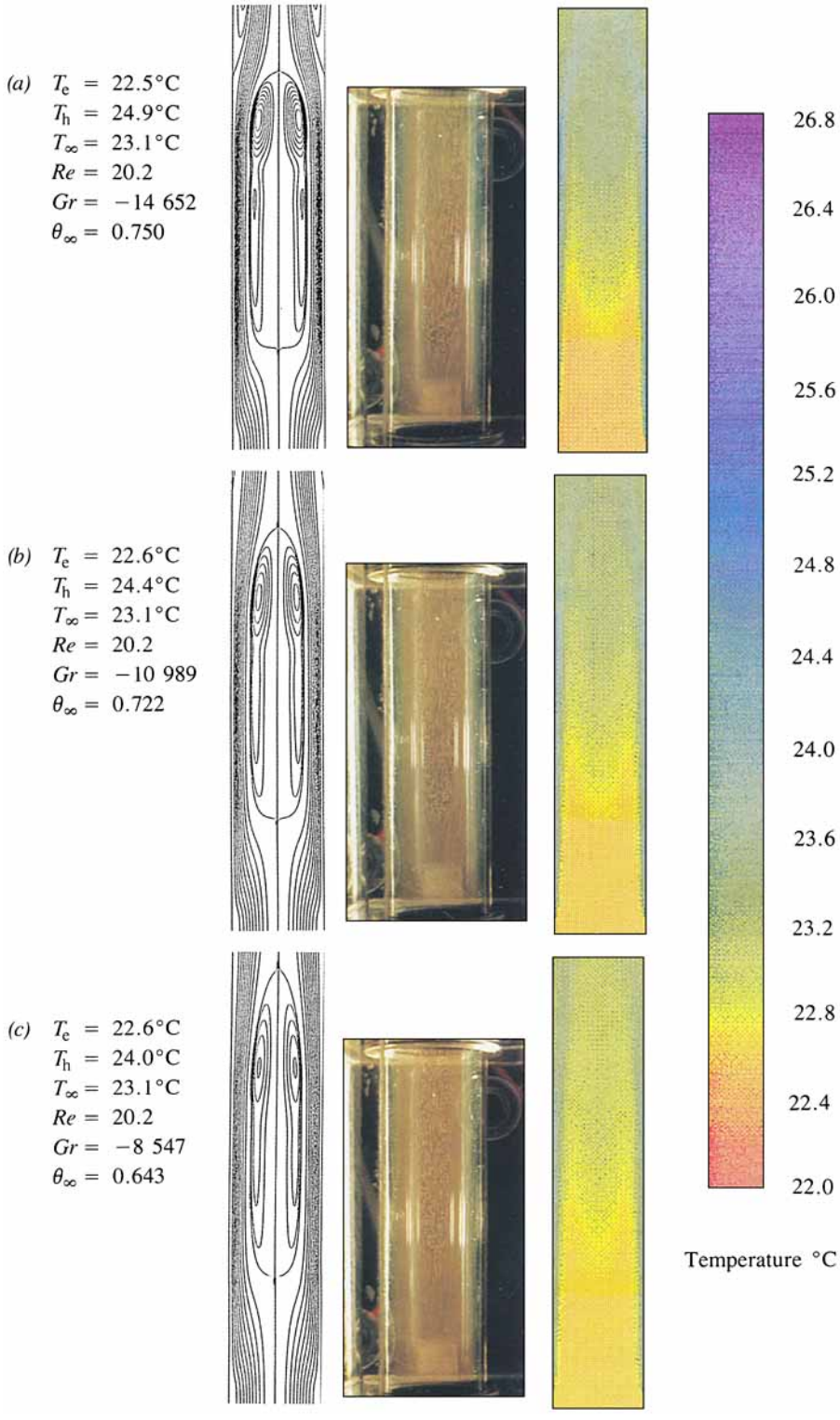

FIGURE 9. Contour plots of stream function, colour photographs from the experiment and colour coded temperature diagrams for the three flow situations in table 3.

recirculating core with axial upflow probably caused because diffusion plays a dominant role in the very slow flow near the primary stagnation point. The warmest fluid below this stagnation point is near the axis, whereas above the stagnation point the slowly recirculating fluid in the inner core is at relatively uniform temperature. This creates the possibility of establishing a very weak inner recirculation by conduction of heat past the stagnation point. The inner recirculation is too weak to see in the streamlines in the experimental photograph in figure 3(*a*).

Although the colours in the temperature diagrams are rather more bold than in the photographs, the numerical simulation of the temperature distributions can be seen to be very good in each of figures 3(*a*), 3(*b*) and 3(*c*).

The flow average temperature, local Nusselt number, average Nusselt number, and Reynolds number times friction factor, respectively, are defined as follows (Morton *et al.* 1987):

$$T_{\mathrm{m}} = -2\int_0^1 \frac{\partial \psi}{\partial R} T \,\mathrm{d}R, \tag{25}$$

$$Nu = -\frac{\partial \theta}{\partial R}\bigg|_{R=1} \Big/ (\theta_{\mathrm{m}} - \theta|_{R=1}), \tag{26}$$

$$Nu_{\mathrm{AV}} = \frac{1}{Z - b/aRe}\int_{b/aRe}^{Z} Nu \,\mathrm{d}Z, \tag{27}$$

$$Ref = 8\Omega|_{R=1}, \tag{28}$$

where Nu_{AV} is calculated between the axial locations b/ARe and Z. Plots of T_{m}, Nu, Nu_{AV} and Ref are displayed in figures 4(*a*), 4(*b*), 4(*c*) and 4(*d*), respectively, for the three flows considered in figure 3. The flow average temperature is seen to drop very little over the first region of the water bath. However, the greater penetration of the wall temperature in the second water bath for the case with $Re = 15.1$, which is apparent from figure 3(*a*), is seen to cause a very much more rapid rise in T_{m} over that part of the tube. From figures 4(*b*) and 4(*c*), a lower Reynolds number is seen to produce more dramatic rises and falls in the Nusselt numbers, implying more efficient heat transfer at low Re, as would be expected. Dramatic rises and falls are also present in the plots of Ref for lower Re, and this is also expected owing to the larger recirculation regions which are apparent from figure 3.

The final three situations to be considered from table 1 are presented in figures 5(*a*), 5(*b*) and 5(*c*) (Plate 2), respectively. Streamlines are plotted for the same values of ψ as in figure 3. In this group the third situation has a low value of Gr but the three cases have almost equal values for $\theta_\infty Gr$. Again the axial stagnation point is higher for experiment than simulation for the two larger Reynolds numbers in figures 5(*b*) and 5(*c*). The disparity is greater than in figures 3(*b*) and 3(*c*) and the fact that stagnation occurs higher in the upper bath supports the view that its cause may be in the difference between experiment and simulation above the upper bath. The recirculation region at the centre of the pipe for the flow in figure 5(*a*) is predicted well and the experimental evidence for the existence of the secondary recirculation at the centre of the pipe is even stronger in this case than for the flow in figure 3(*a*). The shape of the primary recirculation can be seen near its beginning (although it is clearer on an enlarged photograph) and this corresponds closely to the predicted streamlines, supporting the existence of the secondary recirculation. The colour coding for the temperature diagrams is the same as in figure 3. The agreement between the predicted and observed colours is again good, although the red and yellow regions are not quite as well defined in the photographs as in figure 3. In

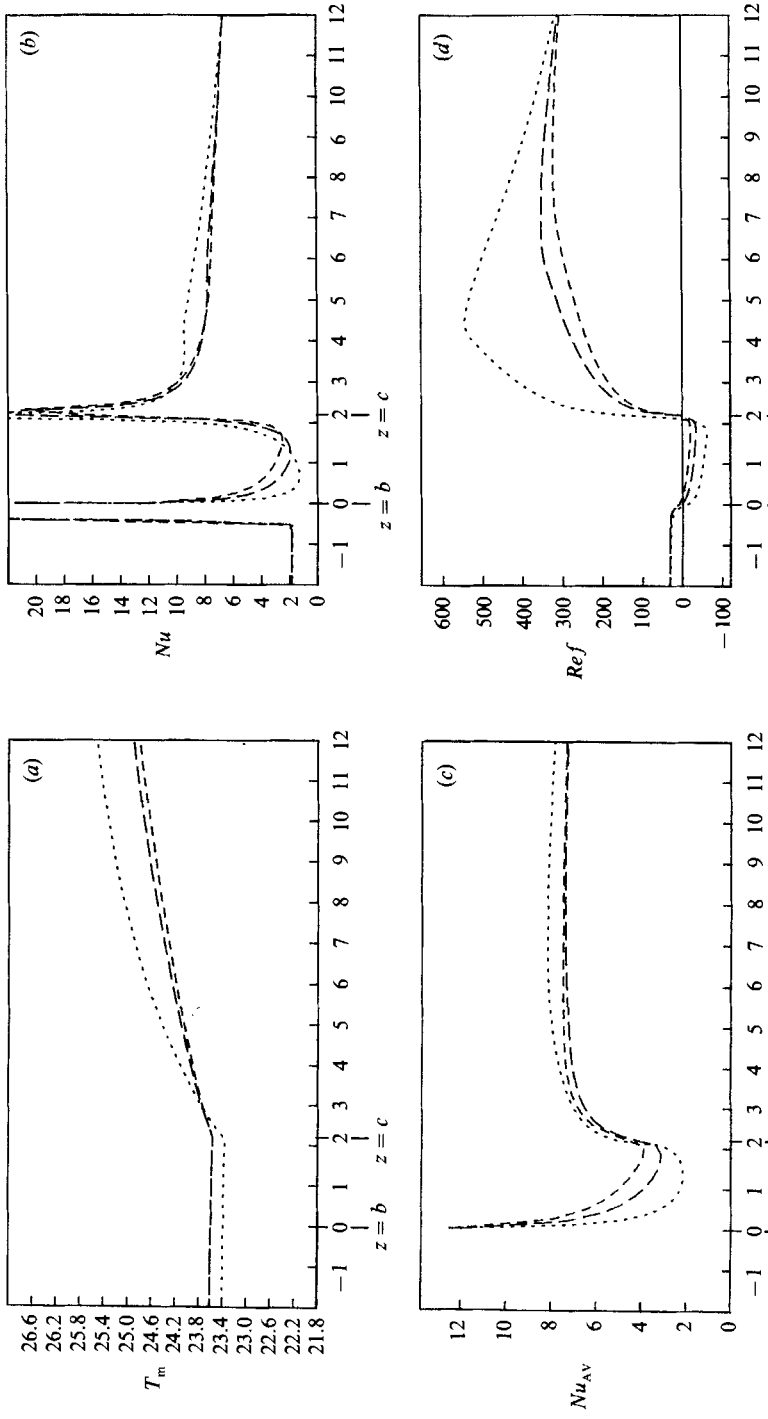

FIGURE 4. (*a*) Average temperature, (*b*) local Nusselt number, (*c*) average Nusselt number, and (*d*) Reynolds number times friction factor for the flows considered in figure 3.

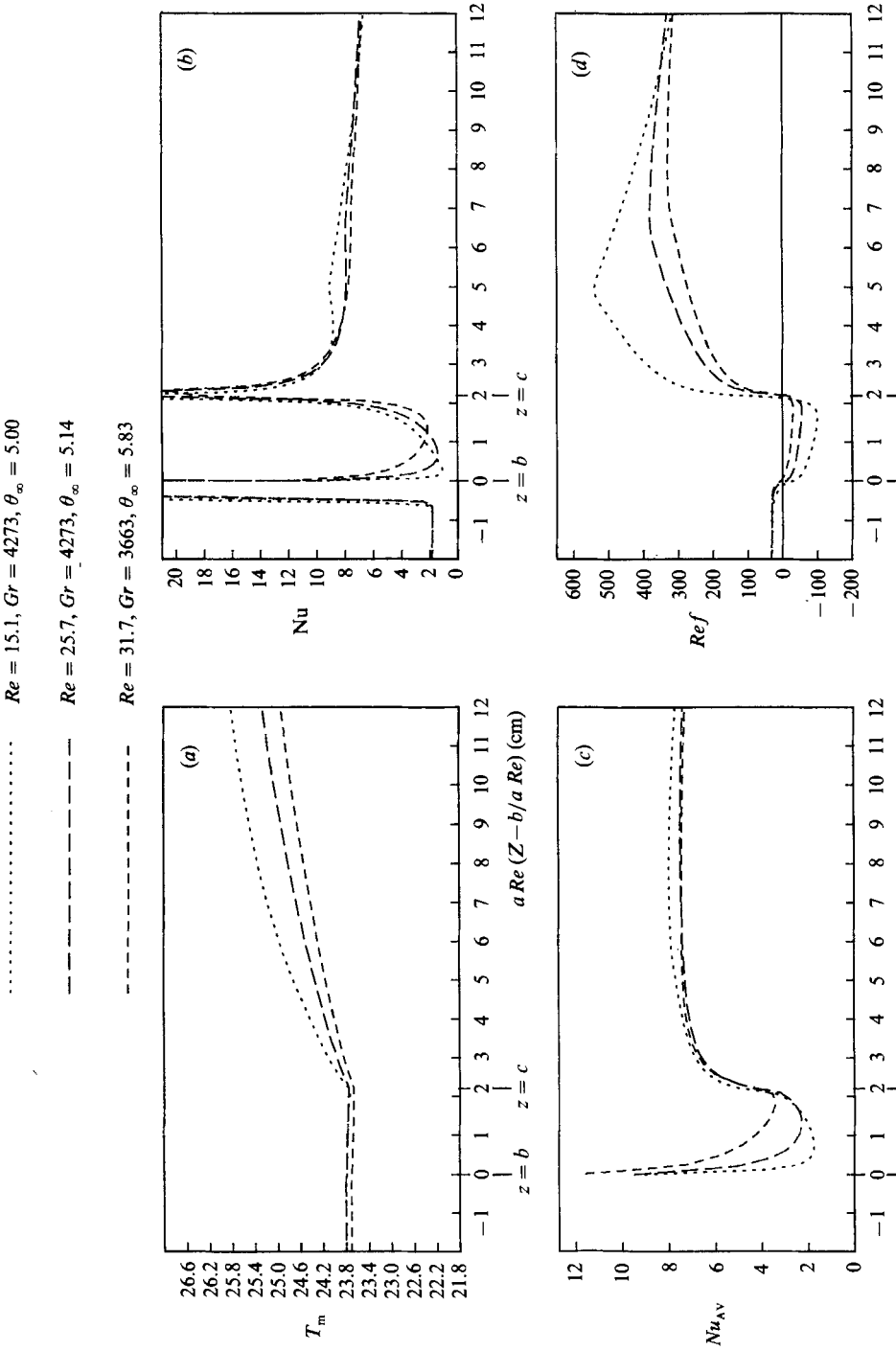

FIGURE 6. (*a*) Average temperature, (*b*) local Nusselt number, (*c*) average Nusselt number, and (*d*) Reynolds number times friction factor for the flows considered in figure 5.

	u_m	T_e	T_h	T_∞	Re	Gr	θ_∞
(*a*)	1.58×10^{-3}	22.0	25.7	22.4	22.3	−22589	0.892
(*b*)	1.28×10^{-3}	22.2	25.7	22.4	18.1	−21368	0.943
(*c*)	1.24×10^{-3}	22.5	25.7	22.5	17.5	−19536	1.000

TABLE 2. Flow data for case (II)

figures 6(*a*), 6(*b*), 6(*c*), and 6(*d*), T_m, Nu, Nu_{AV} and Ref, are displayed, respectively, for the three flows considered in figure 5. The conclusions to be drawn from figure 6 are similar to those drawn from figure 4.

4.2. *Case (II): Heating over the short section followed by cooling over the long section*

The bath configuration is as in case (I) but the order of heating and cooling is reversed; the values of the parameters ν, β and Pr are unchanged. Three situations are considered and the temperatures, velocities and governing non-dimensional parameters for these flows are displayed in table 2.

The three situations considered are presented in figures 7(*a*), 7(*b*) and 7(*c*) (Plate 3), respectively. Streamlines are plotted for the same values of ψ as were used in figure 3. The temperature coding is different from that used in figures 3 and 5 but it was still derived from a set of stationary photographs taken over the indicated range of temperatures. The entry temperature is now varied while the other temperatures are kept approximately constant. Heating in the short bath produces axial stagnation for this range of parameters with acceleration of the working fluid radially outwards into a thin annular upflow near the tube wall. Subsequent cooling in the upper bath generates downward buoyancy near the walls and upward buoyancy reinforcing the pressure gradient near the axis. The thickness of the cool boundary layer in the upper bath depends on the balance between heat conduction (and hence momentum diffusion at fixed Prandtl number) and advection; at the lowest Re reverse flow at the wall penetrates deeply and the axial recirculation is cut off abruptly, while for increasing values of Re the flow reversal retreats progressively further up the wall and the axial recirculation bubble lengthens. The streamlines predicted by the numerical model are seen to correspond fairly closely to the observed streamlines from the photographs. The shape and size of the recirculation region at the centre of the tube is predicted quite well in each case, and the length of this region can be seen to decrease as the Reynolds number decreases and the entry temperature increases. Predicting the point of flow separation from the wall in the second and third flow situations is one of the more stringent tests of the numerical model. It can be seen from figures 7(*b*) and 7(*c*) that there is reasonably good agreement. However, the recirculation regions associated with these flow separations are seen in the experiments to have a less significant effect on the shortening of the recirculation region at the centre of the tube than is predicted by the mathematical model. In this set of experiments the colours in the photographs vary less than in the two earlier investigations and the main points of interest are the green streaks downstream of the first water bath in figure 7(*c*), which are predicted fairly well by the numerical model. Elsewhere there is little change of colour.

In figures 8(*a*), 8(*b*), 8(*c*) and 8(*d*), T_m, Nu, Nu_{AV} and Ref, respectively, are plotted for the three flows considered in figure 7. Note from figure 8(*a*) that the different values of $T_h - T_e$ resulting from the different entry temperatures produce differences

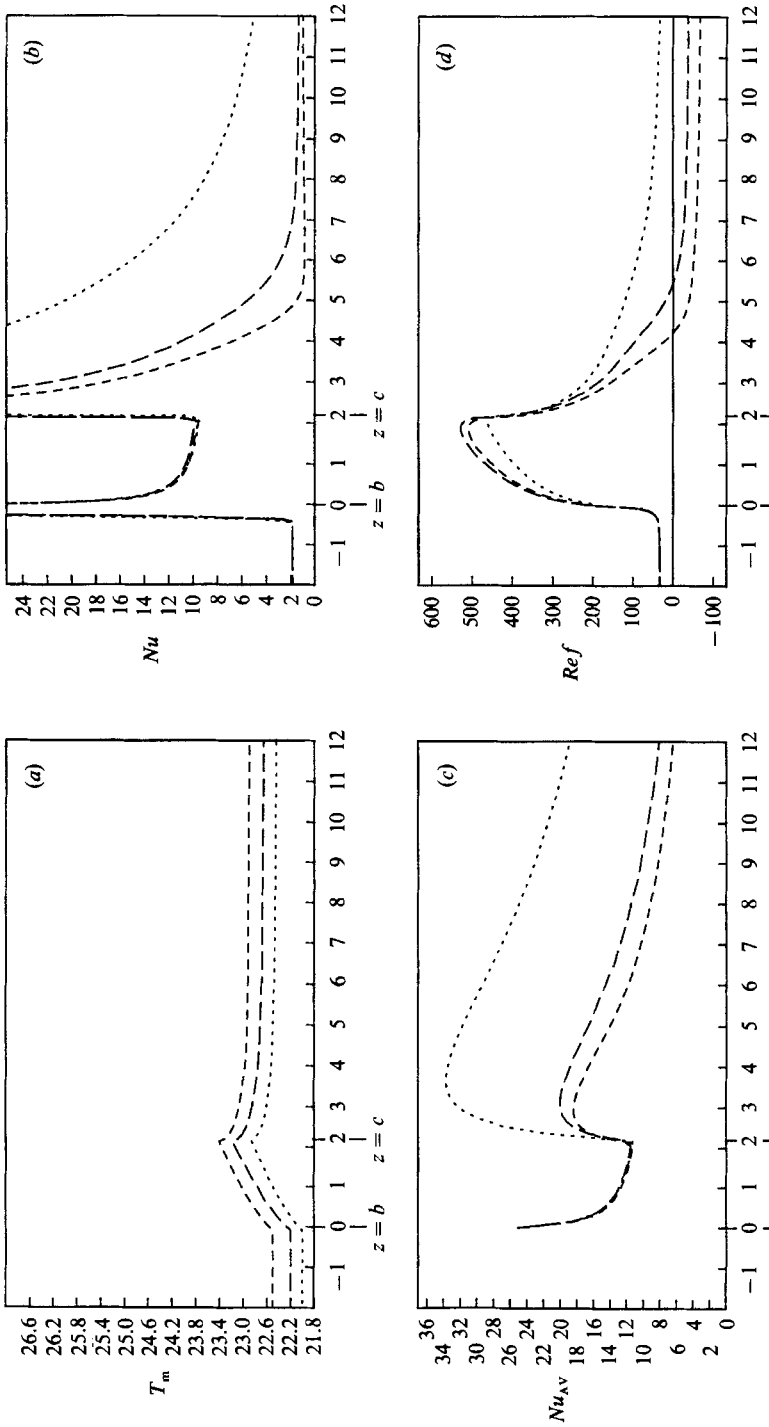

FIGURE 8. (*a*) Average temperature, (*b*) local Nusselt number, (*c*) average Nusselt number, and (*d*) Reynolds number times friction factor for the flows considered in figure 7.

	u_m	T_e	T_h	T_∞	Re	Gr	θ_∞
(*a*)	1.43×10^{-3}	22.5	24.9	23.1	20.2	−14652	0.750
(*b*)	1.43×10^{-3}	22.6	24.4	23.1	20.2	−10989	0.722
(*c*)	1.43×10^{-3}	22.6	24.0	23.1	20.2	−8547	0.643

TABLE 3. Flow data for case (III)

in T_m that survive over the whole of the region covered by the water baths in the experimental investigation. From figures 8(*b*) and 8(*c*), the Nusselt numbers are seen to be almost the same up to the divide in the water bath; however, from that point onwards, the recirculation regions adjacent to the wall of tube and the slow rate at which T_∞ is attained in the second and third flows cause the corresponding Nusselt numbers to be very small. The Reynolds number times the friction factor is also seen to be most affected over the second section of the water bath from figure 8(*d*). This is due to the large recirculation regions present in the second and, in particular, the third of the flows under consideration.

4.3. *Case (III): Heating over the long section followed by cooling over the short section*

For this case the lower bath of length 8.5×10^{-2} m is heated in each situation to approximately 2 °C above ambient and the shorter upper bath is cooled back to about 0.5 °C above ambient. The values of ν, β and Pr are the same as for cases (I) and (II). Three situations are considered and the temperatures, velocities and governing non-dimensional parameters for these flows are displayed in table 3.

As in cases (I) and (II), the region beyond the second section of the water bath is treated as if that part of the bath extends to infinity in the mathematical model. This is a better assumption in this case because the fluid is cooled by the small bath to a temperature which is not far above room temperature.

In these cases Re is held constant and $\theta_\infty Gr$ is altered by changing the value of T_h. The three situations described in table 3 are presented in figures 9(*a*), 9(*b*) and 9(*c*) (Plate 4), respectively. Streamlines are plotted for the same values of ψ as were used in figure 3. The recirculation regions at the centre of the tube are again predicted reasonably accurately, with the beginning of the recirculation being seen to move a little downstream as $\theta_\infty Gr$ decreases in magnitude. For the larger value of $|\theta_\infty Gr|$ the axial recirculation is restricted in length because a wall recirculation region forms downstream after the pipe enters the short cooling bath. Closure of the axial recirculation within the cooling bath occurs outside the region illustrated in figure 9, although there is perhaps evidence in figure 9(*a*) of a slight broadening of the annular wall flow. The temperature diagrams, which are colour coded in the same way as in figure 7, are seen to have more variation in colour than those in figure 7. The thermal boundary layers adjacent to the pipe wall are clearly visible and the core temperatures appear to be predicted relatively well with, in particular, the light green area at the centre of the tube near the end of the longer bath being clearly observed in the photograph in figure 9(*a*). In figures 10(*a*), 10(*b*), 10(*c*) and 10(*d*), T_m, Nu, Nu_{AV} and Ref, respectively, are displayed for the three flows considered in figure 9. The value of T_h can be seen to be a dominant factor in the value of T_m downstream of the first water bath. This produces phenomena similar to those observed in figure 8 downstream of the heated section. The difference in figure 10 is that variations occur also over the longer first section of the water bath. The trends are as would be

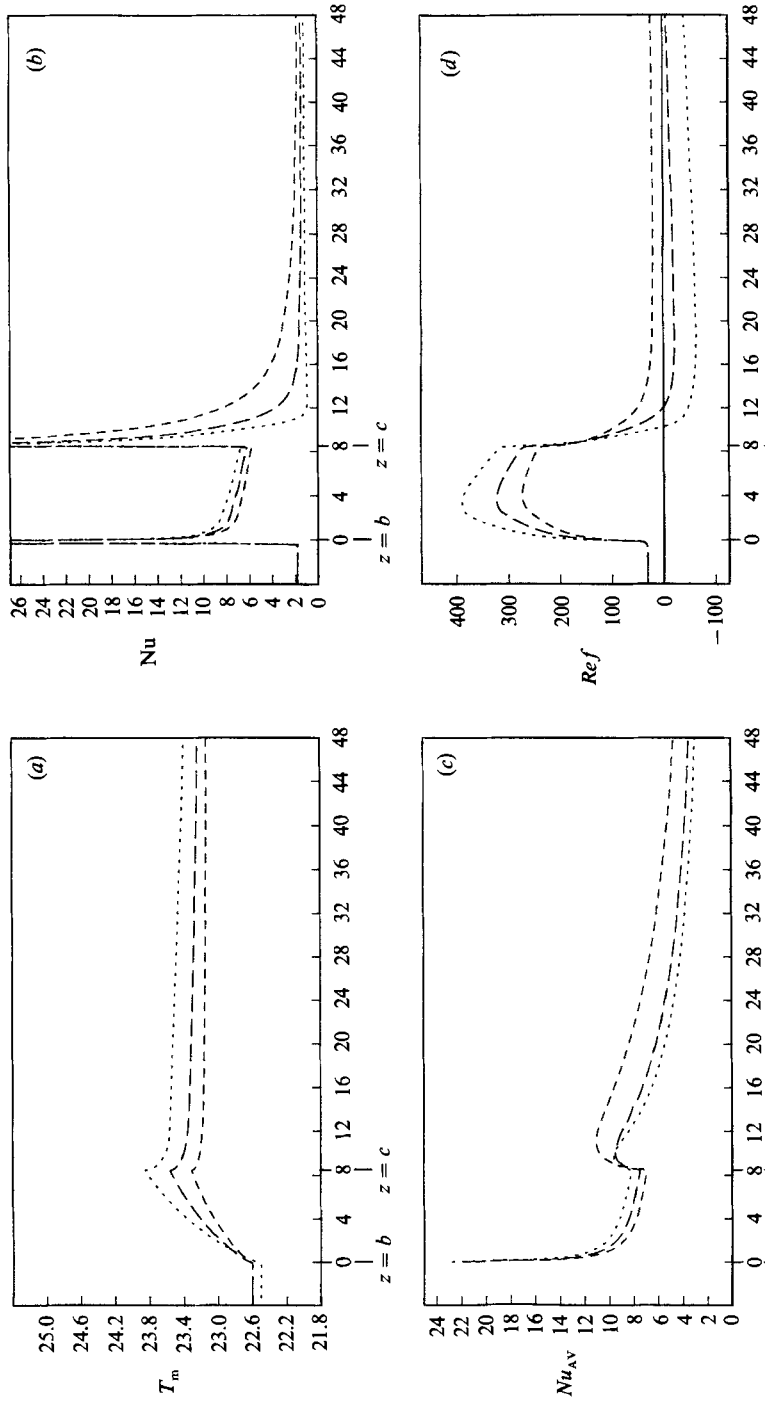

FIGURE 10. (*a*) Average temperature, (*b*) local Nusselt number, (*c*) average Nusselt number, and (*d*) Reynolds number times friction factor for the flows considered in figure 9.

expected with the most extreme variations of Nu, Nu_{AV} and Ref occurring for the larger value of $|\theta_\infty Gr|$.

5. Conclusions

A striking new series of axisymmetric mixed-convection flows have been demonstrated in which interior stagnation and flow recirculation were produced within pressure-gradient-forced flow up a vertical pipe with heated and cooled wall sections. These investigations yield considerable insight into flows in which two competing systems of interior force combine to produce with viscosity a rich and varied set of flow patterns. The flows are of both theoretical and practical interest.

The investigation was by both numerical simulation and laboratory experiment and the two approaches gave results that are in excellent general agreement.

The laboratory experiments used aluminium powder to visualize the streamlines in steady flow, and suspensions of temperature-sensitive liquid crystal particles to give a general indication of the temperature fields. Photographs are presented for several flow configurations.

The numerical study involved the solution of finite-difference equations derived from the governing system of elliptic differential equations using multigrid techniques. In spite of the fact that there are temperature singularities in the boundary conditions, the multigrid solutions were up to seven times faster than single-grid solution routines. For some flows, interesting features which are not apparent from the experimental photographs were revealed by the numerical results.

Possible improvements on the numerical side of the investigation could be achieved by the use of higher-order finite-difference equations or higher-order interpolation routines, and also the accuracy of the solutions could be improved in areas of rapid change by the use of adaptive meshing techniques.

We should like to acknowledge the invaluable contribution of Mr Terry Long, of the Monash Geophysical Fluid Dynamics Laboratory, to the experimental side of this work. D. J. Keen thanks the SERC for providing a research studentship for the duration of his studies.

Appendix

A.1. *Multigrid theory*

The general theory of multigrid techniques and the FAS (Full Approximation Storage) method is covered comprehensively by Brandt (1977). The following, which is similar to the particular approaches of Falle & Wilson (1988) and Gaskell *et al.* (1988), is a summary of the approach adopted for this particular problem.

Consider the systems $\mathrm{L}U = F$ and $\Lambda U = \Phi$ on the domain Ω and its boundary $\partial\Omega$, respectively, where U is a variable on Ω and $\partial\Omega$, L and Λ are differential operators and F and Φ are source terms. These systems can be discretized on a grid G^k, approximating Ω, as follows:

$$\mathrm{L}^k U^k = F^k, \tag{A 1}$$

$$\Lambda^k U^k = \Phi^k, \tag{A 2}$$

where L^k and Λ^k are difference operators and U^k, F^k and Φ^k are the discrete

approximations to U, F and Φ on G^k. Now if u^k is an approximation to U^k (think of U^k as being converged and u^k as being unconverged from now on) then

$$\mathrm{L}^k u^k = F^k - f^k, \tag{A 3}$$

$$\Lambda^k u^k \Phi^k - \phi^k, \tag{A 4}$$

where f^k and ϕ^k are the residuals, or the amounts by which u^k fails to satisfy (A 1) and (A 2), respectively. From now on a capital U is used to refer to a converged finite-difference solution and a small u is used to refer to an unconverged finite-difference solution. Now suppose there exist two grids G^h and G^H with mesh sizes h and H such that $H = 2h$. One way to obtain a good approximation, u^h, on the finer grid, G^h, is first to obtain a solution, U^H, on the coarser grid, G^H; $\mathrm{L}^H U^H = F^H$, and then interpolate to the fine grid:

$$u^h = I_H^h U^H, \tag{A 5}$$

where I_H^h represents a prolongation from G^H to G^h. This idea can be extended to obtain the G^H solution from even coarser grids; however, this theory does not exploit the proximity of G^H to G^h. Using multigrids, not only can a first guess to u^h be generated using G^H, but improvements to u^h can also be achieved. In order to improve u^h the error function V^h must be used, where

$$V^h = U^h - u^h. \tag{A 6}$$

If U^h is not smooth on scales of order-h then, for arbitrary u^h, V^h will not be smooth. However, after a few relaxation sweeps on G^h the high-frequency error components of V^h will be destroyed. At this point convergence slows down and coarser grids must be used. Assuming a coarser grid, G^H, has been used, V^h can be approximated by V^H as follows:

$$V^h = I_H^h V^H \tag{A 7}$$

and then u^h can be updated:

$$(uh)^{\mathrm{new}} = (uh)^{\mathrm{old}} + I_H^h V^H. \tag{A 8}$$

The residual equations satisfied by V^h when L is nonlinear are as follows:

$$\hat{\mathrm{L}}^h V^h = r^h, \tag{A 9}$$

where $\hat{\mathrm{L}}^h V^h = \mathrm{L}^h(u^h + V^h) - \mathrm{L}^h(u^h)$ and $r^h = F^h - \mathrm{L}^h(u^h)$. Similar equations exist on the boundary, but for convenience they will be ignored from now on since they are of the same form as the interior equations.

A.2. *The FAS method*

The problem is solved using a scheme known as the full approximation storage (FAS) method. This is carried out as follows; approximate equation (A 9) on G^H as follows:

$$\mathrm{L}^H(I_h^H u^h + V^H) - \mathrm{L}^H(I_h^H u^h) = I_h^H r^h, \tag{A 10}$$

where I_h^H represents a contraction from G^h to G^H. Now introduce the new variables

$$u_H^h \equiv I_h^H u^h + V^H. \tag{A 11}$$

These new variables represent, on the coarse grid, the sum of the basic approximation, which can be thought of as being fixed, plus its correction V^H. Equation (A 10) now becomes

$$\mathrm{L}^H u_h^H = F_h^H = \mathrm{L}^H(I_h^H u^h) + I_h^H r^h. \tag{A 12}$$

Equation (A 12) has the advantage that it resembles the original equation (A 9) except for a different right-hand side, so the same relaxation routine can be used on all levels. The approximation u^h on G^h is corrected by solving (A 12) (or approximately solving it), and interpolating V^H onto G^h, updating u^h as indicated in (A 8).

When convergence is achieved $u^h = U^h$ and $V^h = 0$ so that

$$u_h^H = I_h^H U^h, \tag{A 13}$$

i.e. u_h^H is a coarse grid function which coincides with the projection of the fine grid solution. The above theory can be extended to three or more grids.

A.3. *The solution algorithm*

The above theory is applied to the duct problem in the following manner. Suppose an unconverged solution u^M exists on G^M, the finest grid, with the coarser grids being represented by $G^0, G^1, \ldots, G^{M-1}$, and the grid size ratio of G^{k+1} to G^k being equal to $\frac{1}{2}$. Here u represents each of the variables ψ, Ω and θ. Proceed as follows:

(i) Interpolate u^M and r^M to each of the coarser grids. The correction equations are determined from (A 12) to be

$$\mathrm{L}^k u^k = \bar{F}^k, \tag{A 14}$$

where

$$\bar{F}^k = \mathrm{L}^k(I_{k+1}^k u^{k+1}) + I_{k+1}^k(\bar{F}^{k+1} - \mathrm{L}^{k+1} u^{k+1}), \quad k \neq M; \quad \bar{F}^M = F^M; \quad u^k = I_M^k u^M$$

plus the boundary conditions.

(ii) On each grid start with u^k as an initial state and perform one iteration.

(iii) Start iterating on the grid that is most efficient at converging the solution. This is the grid on which the quantity

$$\|\{u^k\}^{n+1} - \{u^k\}^n\| \tag{A 15}$$

is largest. Here $n+1$ and n refer to two consecutive iterations and $\|\cdot\|$ is the 2-norm. The quantity (A 15) is generally, though not always, largest on the coarsest grid.

(iv) Assuming that (A 15) is largest on G^k, iterations are carried out using (A 14) on G^k until convergence slows down or the residual has decreased by a predetermined amount.

(v) The correction, which is given by

$$V^k = (u^k)^{\mathrm{new}} - (u^k)^{\mathrm{old}}, \tag{A 16}$$

is interpolated to the next finite-difference grid, G^{k+1}, where u^{k+1} is updated according to (A 8).

(vi) Iterate on G^{k+1} and then correct to G^{k+2}, and so on to G^M.

(vii) Iterate on G^M until convergence slows down (usually only a few iterations).

Steps (i)–(vii) constitute one multigrid cycle.

The approximation to the present problem, at any particular multigrid level, is obtained iteratively by sweeping across the grids G^Z and G^ξ from $Z = 0$ *to* $\xi = 1$, relaxing the relevant finite-difference equations, for each of the variables ψ, Ω and θ in turn, at every point on the two grids during each sweep. The relaxation parameters used for each of the finite-difference variables ψ, Ω and θ are different, with Ω and θ needing to be under relaxed, Ω more so than θ, and ψ having a relaxation parameter of unity. It is also found that smaller relaxation parameters for Ω and θ are necessary as the grids become coarser, in order to avoid divergence on

these coarse grids. The relaxation parameters for Ω and θ are dependent upon the size of Re, with smaller values being needed as Re becomes larger.

A problem encountered on the coarser multigrid levels is the matching of the solution between the grids G^Z and G^ξ at $Z = d$. This is overcome by using a third relaxation routine, valid along $Z = d$ (which is incorporated into each iterative sweep for the row of finite-difference points along $Z = d$) where the axial derivative terms are expressed in terms of the two axial steps either side of $Z = d$ (these steps only being equal on the finest mesh). On G^ξ care must be taken to determine the correct governing equations if each point on a coarse mesh is to correspond to a point on the next fine mesh. In order to illustrate this consider the penultimate fine mesh, G^{M-1}. The expression

$$\xi^* = 1 - 1/(1 + C^*(Z^* - d)) \tag{A 17}$$

is valid on G^{M-1}, where * refers to values on G^{M-1}. Thus the following must hold:

$$\xi^*_{NN/2+2} = 1/\tfrac{1}{2}N^\xi = 1 - 1/(1 + C^*(Z^*_{NN/2+2} - d)). \tag{A 18}$$

It must be true that $Z^*_{NN/2+2} = Z_{NN+3}$ and $\xi^*_{NN/2+2} = \xi_{NN+3}$, so (A 18) can be expressed as follows:

$$2/N^\xi = 1 - 1/(1 + C^*(Z_{NN+3} - d)). \tag{A 19}$$

Z_{NN+3} can be determined from (24), and substitution into (A 19) leads to a value for C^* of

$$C^* = 1/((N^\xi - 1)K), \tag{A 20}$$

which is identical to the value of C given by (23). The value of C can be shown to be the same on all coarse grids, hence the relaxation routines used on the coarse meshes for $Z > d$ are exactly the same as those used on the fine mesh G^ξ.

The fine to coarse interpolation function, I^k_{k+1}, is taken to be the 9-point restriction used by Ghia *et al.* (1982). That is, the value of a finite-difference variable at the point $(i+1, j+1)$ on the coarse mesh, take for instance ψ, is given as follows:

$$\begin{aligned}(I^k_{k+1}\psi^{k+1})_{i+1,j+1} = {} & \tfrac{1}{4}\psi^{k+1}_{2i+1,2j+1} + \tfrac{1}{8}[\psi^{k+1}_{2i+2,2j+1} + \psi^{k+1}_{2i+1,2j+2} + \psi^{k+1}_{2i,2j+1} + \psi^{k+1}_{2i+1,2j}] \\ & + \tfrac{1}{16}[\psi^{k+1}_{2i+2,2j+2} + \psi^{k+1}_{2i,2j+2} + \psi^{k+1}_{2i+2,2j} + \psi^{k+1}_{2i,2j}].\end{aligned} \tag{A 21}$$

This interpolation is not as important as the coarse to fine interpolation given by I^{k+1}_k because of the large gradients present at certain points in all of the flows considered. The linear form of I^{k+1}_k used by Ghia *et al.* (1982) was found to be less suitable, for the flows considered here, than a third-order upwind scheme which uses a weighted average of the two coarse grid points either side of a new fine grid point and the next upwind point on the coarse grid. This can be represented as follows, for a forward flow in the axial direction:

$$\begin{aligned}(I^{k+1}_k\psi^k)_{2i+1,2j+1} &= \psi^k_{i+1,j+1}, \\ (I^{k+1}_k\psi^k)_{2i+1,2j+2} &= \tfrac{3}{8}\psi^k_{i+1,j+2} + \tfrac{3}{4}\psi^k_{i+1,j+1} - \tfrac{1}{8}\psi^k_{i+1,j},\end{aligned} \tag{A 22}$$

with similar expressions being valid for reverse flows and for interpolations in the radial direction.

REFERENCES

BRANDT, A. 1977 Multi-level adaptive solutions to boundary value problems. *Maths Comput.* **31**, 333–390.

COLLINS, M. W. 1975 Viscous dissipation effects on developing laminar flow in adiabatic and heated tubes. *Proc. Inst. Mech. Engrs* **189**, 129–137.

FALLE, S. A. E. G. & WILSON, M. J. 1988 Multigrid calculation of jet flow. In *ICFD Conf. on Numerical Methods for Fluid Dynamics*. IMA Conference Series. Clarendon.

FUCHS, L. 1986 A local mesh-refinement technique for incompressible flows. *Computers Fluids* **14**, 69–81.

GASKELL, P. H., LAU, A. K. C. & WRIGHT, N. G. 1988 Comparison of two solution strategies for use with higher order discretisation schemes in fluid flow simulation. *Intl J. Numer. Meth. Fluids* (to appear).

GHIA, U., GHIA, K. N. & SHIN, C. T. 1982 High-*Re* solutions for incompressible flow using the Navier–Stokes equations and a multigrid method. *J. Comput. Fluids* **48**, 387–411.

GRAY, D. D. & GIORGINI, A. 1976 The validity of the Boussinesq approximation for liquids and gases. *Intl J. Heat Mass Transfer* **19**, 545–551.

KEEN, D. J. 1988 Combined convection in heat exchangers. Ph.D. thesis, University of Leeds.

MORTON, B. R. 1960 Laminar convection in uniformly heated vertical pipes. *J. Fluid Mech.* **8**, 227–240.

MORTON, B., INGHAM, D. B., KEEN, D. J. & HEGGS, P. J. 1987 Experimental and numerical investigations into recirculating combined convection in laminar pipe flow. *Proc. Intl Symp. on Natural Circulation, ASME Winter Annual Meeting, Boston, MA, Dec. 1987*, pp. 331–339.

PHILLIPS, R. E. & SCHMIDT, F. W. 1985 A multilevel-multigrid technique for recirculating flows. *Numer. Heat Transfer* **8**, 573–594.

RAZNJEVIC, K. 1976 *Handbook of Thermodynamic Tables and Charts*. McGraw-Hill.